Interval Estimation of Binomial Proportion in Clinical Trials with a Two-Stage Design

Wei-Yann Tsai[1], Yunchan Chi[2,*], Chia-Min Chen[2]

[1]Department of Biostatistics, Columbia University, New York City, New York, U.S.A
[2]Department of Statistics, College of Management, National Cheng Kung University
ycchi@stat.ncku.edu.tw

1. Introduction

In a drug development process, the primary goal of Phase II clinical trials is to determine whether there is sufficient evidence of efficacy and safety to make it worth further study in a Phase III clinical trial. For example, suppose a new drug is developed for patients with liver cancer. To investigate whether this new drug extends the life of liver cancer patients, the criterion of drug efficacy is defined to be the presence of tumor shrinkage, which is a binary endpoint with response probability p. In a single-stage design, if the number of patients with tumor shrinkage is large enough, then this new drug may be used as evidence for further testing.

Most often, drug experiments employ a Simon's two-stage design [1] in order to avoid giving patients an ineffective drug. Suppose there are n_1 patients participating in the first-stage experiment, and there are n_2 additional patients participating in the second-stage experiment if the new drug design is allowed to continue. The number of responses Y_1 is observed at the first stage, and if Y_1 is less than a specified value a, the design is stopped. Otherwise, this drug design is allowed to continue and the number of responses Y_2, which is independent of Y_1, is observed at the second stage. Consequently, the response probability of patients with tumor shrinkage is to be estimated in order to plan a further study.

It is natural to use sample proportion $\tilde{p} = (Y_1 + Y_2)/(n_1 + n_2)$ to estimate p. However, when the second stage is allowed to continue, this estimator will overestimate the true p, because the number of responses at the first stage is truncated by a and follows a truncated binomial distribution. Therefore, a maximum likelihood estimator based on the truncated binomial distribution is derived to take into account the truncation effect. In addition, to take into account the inherent variability of patients in the measured responses, the confidence interval, that is a range of feasible values within which the true p may lie, is also constructed for p. Two types of interval estimators, the Wald interval without (with) continuity correction [2] and the score interval without (with) continuity correction [3], are constructed in the next section.

2. The proposed method

When the second stage is allowed to continue, the possible values of Y_1 are truncated by a, so the probability distribution of Y_1 is referred to as truncated binomial distribution with response probability p and its probability mass function is

$$P_a(Y_1 = y_1) = \frac{\binom{n_1}{y_1} p^{y_1}(1-p)^{n_1-y_1}}{\sum_{k=a}^{n_1} \binom{n_1}{k} p^k (1-p)^{n_1-k}}$$

with $y_1 = a, a+1, \dots, n_1$. While the probability distribution of Y_2 is binomial with the same response probability p, and its probability mass function is

$$P(Y_2 = y_2) = \binom{n_2}{y_2} p^{y_2}(1-p)^{n_2-y_2}$$

where $y_2 = 0, 1, 2, \dots, n_2$. Let $\log L(p) = \log(P_a(Y_1 = y_1) P(Y_2 = y_2))$ denote the logarithm of likelihood function based jointly on $Y_1 = y_1$ and $Y_2 = y_2$ and its first derivative with respective to p is $U(p)$. Note that the maximum likelihood estimator of p is the solution to $U(p) = 0$. The graph of $U(p)$ displays that a unique solution can be obtained for $a < y_1 + y_2 < n_1 + n_2$ and the equation $U(p) = 0$ does not have a closed-form solution. Hence, the Newton-Raphson algorithm is employed to obtain a numerical estimate of p and the iteration equation $p_{[j]} = p_{[j-1]} + U(p_{[j-1]}) / J(p_{[j-1]})$, where the observed Fisher information, $J(p)$, must be derived as the negative of the second derivative of $\log L(p)$ with respective to p. Note that the iterations proceed until difference between $p_{[j]}$ and $p_{[j-1]}$ is smaller than a required error tolerance level (say, 10^{-4}).

Next, the interval estimators for p are constructed as follows. By the property of maximum likelihood estimator, the statistic $(\hat{p} - p)/I^{-1/2}(\hat{p})$ has an asymptotic standard normal distribution, where the Fisher information of $\hat{p}$, $I(p)$, is the expectation of $J(p)$. Consequently, the lower and upper limits of a two-sided Wald interval for p are given by solving the equations of the expression $(\hat{p} - p)/I^{-1/2}(\hat{p}) = z_{\alpha/2}$ and $(\hat{p} - p)/I^{-1/2}(\hat{p}) = \cdot z_{\alpha/2}$; respectively, where $z_{\alpha/2}$ is the $100(1-\alpha/2)$ th percentile of the standard normal distribution. The resulting Wald interval (Wald) is denoted by $[\hat{p} - z_{\alpha/2}I^{-1/2}(\hat{p}), \hat{p} + z_{\alpha/2}I^{-1/2}(\hat{p})]$. Because a discrete random variable can take on only specified values, the correction for continuity adjustment, $1/(2(n-a))$, is employed. The resulting Wald interval with continuity correction (Wald_c) is denoted by $[\hat{p} - (z_{\alpha/2}I^{-1/2}(\hat{p}) + 1/(2(n-a)) \, \hat{p} + (z_{\alpha/2}I^{-1/2}(\hat{p}) + 1/(2(n-a))$ Following Wilson's [3] concept, the lower and upper limits of the score confidence interval without (with) continuity correction can also be solved by replacing $\hat{p}$ with the actual success probability p. So for given $\hat{p}$, the lower and upper limits of the score interval are the solution to the equations $(\hat{p} - p) - z_{\alpha/2}I^{-1/2}(p) = 0$ and $(\hat{p} - p) + z_{\alpha/2}I^{-1/2}(p) = 0$ respectively. The

resulting confidence interval (*Score*) is denoted by $\left[p_L^{Score}, \quad p_U^{Score}\right]$. Similarly, the score interval with continuity correction (*Score_c*) is denoted by $\left[p_L^{Score\_c}, \quad p_U^{Score\_c}\right]$.

3.Comparison results

The evaluation criteria for comparing the performance of interval estimators are the actual coverage probability and the expected width of an interval estimator, which is defined as $CP(p)=\sum I(x,p)P(X=x)$ and $EW(p) = \sum (\hat{p}_U - \hat{p}_L)P(X = x)$, respectively, where $I(x, p)$ is an indicator with 1 if the interval based on $X=x$ contains p, and 0 if it does not contain p and $\hat{p}_U - \hat{p}_L$ is the width of an interval estimate. Note that the length of confidence interval measures the precision of estimation, and it is desirable to obtain a confidence interval that is short enough with adequate confidence (or coverage probability).

In Phase II clinical trials, the investigators are asked to specify the largest (smallest) success probability, p_1 (p_0), which, if true, would clearly imply that the treatment is (is not) promising for further study. For given p_0, p_1, α, and β (type II error rate), Table I displays the actual coverage probabilities and the expected width. In this sense, the maximum likelihood estimator of p is slightly underestimated and the sample proportion is overestimated. When n_1 is considerably larger than n_2, for example, n_1=34 and n_2=5, the maximum likelihood estimator $\hat{p}$ underestimates significantly the true p and the coverage probability of the score interval without continuity correction is considerably lower than the nominal confidence level which is 0.95 in this comparison. Although the expected interval width of the score interval without continuity correction is almost the smallest, the difference between the expected interval widths of two score interval estimators is negligible. Therefore, according to the mean coverage probability and expected interval width, this paper recommended the score interval with continuity correction for estimating p based on the data from Simon's two-stage designs.

Table I. The coverage probabilities, expected interval width and biases for Simon's designs with α= 0.05 and β= 0.2 for p_1-p_0= 0.2

n_1	n_2	a	p_0/p_1	Interval estimators				Expected interval width				Point estimators	
				Wald	Wald_c	Score	Score_c	Wald	Wald_c	Score	Score_c	$\hat{p}$	$\tilde{p}$
12	4	1	0.05	0.3934	0.3951	0.9848	0.9848	0.1145	0.1280	0.2576	0.2625	−0.0044	0.0441
			0.25	0.9306	0.9509	0.9306	0.9306	0.3964	0.4466	0.3885	0.3942	−0.0059	0.0061
15	10	2	0.10	0.7886	0.7886	0.9791	0.9791	0.2047	0.2247	0.2496	0.2522	−0.0046	0.0426
			0.30	0.9128	0.9128	0.9627	0.9627	0.3624	0.4030	0.3445	0.3479	−0.0043	0.0053
18	15	5	0.20	0.8914	0.8914	0.9531	0.9531	0.3119	0.3389	0.2946	0.2969	−0.0050	0.0644
			0.40	0.9150	0.9676	0.9345	0.9345	0.3569	0.3924	0.3392	0.3420	−0.0059	0.0115
19	20	7	0.30	0.9084	0.9268	0.9687	0.9687	0.3397	0.3700	0.3116	0.3137	−0.0044	0.0573
			0.50	0.9427	0.9427	0.9589	0.9589	0.3342	0.3655	0.3234	0.3258	−0.0047	0.0094
34	5	18	0.40	0.9387	0.9387	0.9612	0.9612	0.5221	0.5584	0.4007	0.4029	−0.0330	0.1357
			0.60	0.9353	0.9644	0.8535	0.9400	0.4071	0.4535	0.4336	0.4410	−0.0250	0.0210
23	14	13	0.50	0.9248	0.9568	0.9432	0.9432	0.4220	0.4633	0.3815	0.3848	−0.0101	0.0707
			0.0	0.9417	0.9700	0.9488	0.9488	0.3243	0.3658	0.3390	0.3426	−0.0072	0.0073
13	22	9	0.60	0.9358	0.9586	0.9540	0.9540	0.3751	0.4135	0.3503	0.3533	−0.0028	0.0537
			0.80	0.9156	0.9272	0.9336	0.9503	0.2806	0.3166	0.2866	0.2894	−0.0033	0.0088
23	3	20	0.70	0.7153	0.9597	0.9809	0.9809	0.6143	0.6998	0.4807	0.4848	−0.0429	0.1635
			0.90	0.9122	0.9122	0.9178	0.9178	0.3229	0.3997	0.5546	0.5634	−0.0327	0.0205
				0.8689	0.8982	0.9478	0.9543	0.3556	0.3962	0.3587	0.3623	−0.0121	0.0451

References

1. Simom R. Optimal two-stage designs for Phase II clinical trials. *Controlled Clinical Trials* 1989; 10:1-10.
2. Casella G, Berger R. *Statistical inference*. Duxbury: Pacific Grove, 2002.
3. Wilson EB. Probable inference, the law of succession, and statistical inference. *American Statistical Association* 1927; 22:209-212.

Blending of poly(3,4-ethylenedioxythiophene) poly(styrenesulfonate) with poly (ethyleneimine) as an active layer in depletion-mode organic thin film transistors

Yu-Ju Lin[1], Yu-Chang Li[1], Ten-Chin Wen[2], Li-Ming Huang[2], Hong-Jian Yeh[1], Ying-Kuo Chen[3], Yeong-Her Wang[1,*]

[1]Institute of Microelectronics, Department of Electrical Engineering, National Cheng Kung University, Tainan, 701 Taiwan

[2]Department of Chemical Engineering, National Cheng Kung University, Tainan, 701 Taiwan

[3]Institute of Electro-Optical Science and Engineering, National Cheng Kung University, Tainan, 701 Taiwan

yhw@eembox.ncku.edu.tw

With their high potential in terms of flexibility, easy process, and low cost, organic semiconductor have been developed for thin film transistor (TFT) applications. Doped poly(3,4-ethylenedioxythiophene) (PEDOT) displays conductivities ranging from 1-100 S/cm depending on the counter ions. With poly(styrene sulfonic acid) (PSS) as the counter ion, the conductivity is typically 10 S/cm. PEDOT-PSS are heavily exploited as charge injection layers, optically transparent electrodes in polymer light-emitting diodes, as well as conducting elements in organic transistors. However, no other reports can be found for the modulation of conductivity as transistor active layers. In this work, the modulation of conductivity of PEDOT is applied to organic thin film transistor (OTFT).

Fig. 1 shows the schematic diagram of the proposed OTFT on a Si (100) substrate based on PEDOT-PSS with PEI. Fig. 2 illustrates the current–voltage (I-V) characteristics of OTFT. The gate voltage is from 0 to 100V with 20V per step, while the drain voltage is from 0 to 12.5V. Under V_{gs} = 0 V, the drain current (I_{ds}) rises with the drain voltage (V_{ds}) and shows a large current because the active layer made of high doping of PSS in PEDOT leads to a high conducting state.
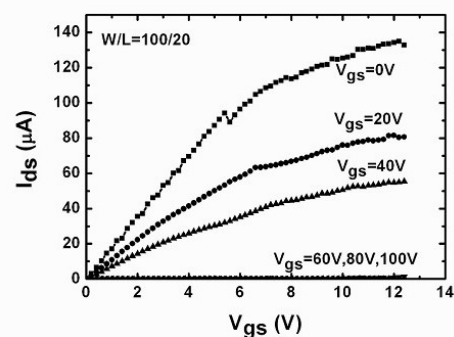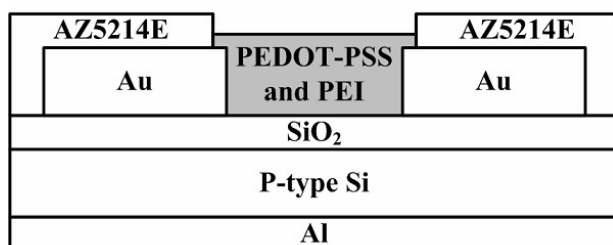
Fig 1. The schematic diagram of the proposed PEDOT-PSS with PEI transistor.

Fig 2. I-V characteristics of the proposed PEDOT-PSS with PEI OTFT.

When a positive voltage is applied to the gate, the currents of the source and drain are decreased. The decreased current for PEDOT-PSS-PEI OTFT is related to the tendency of SO_3^- groups of PSS linking with NH_3^+ of PEI at the applied positive gate voltage as shown in Fig. 3a. When a positive bias is applied to the gate and induces the electric field in the channel, the linked matters (PEI and PSS) are removed from the PEDOT (Fig. 3(b)) and possess low conductivity. This is because the charge carriers have been localized in the sulfur atoms. Therefore, the source-drain current of PEDOT-PSS-PEI-based OTFT is lower than that based on the doped PEDOT under the same source-drain voltage. The stronger the electric fields applied, the more PSS were removed. In other words, applying larger voltages to the gate lowers the presence of source-drain currents. At last, the source-drain currents decreased to $10^{-7} \sim 10^{-8}$ A under V_{gs}=100V (i.e., the OTFTs based on PEDOT-PSS with PEI operating as depletion-mode transistors) as shown in Fig. 2. The on/off ratios are about 10^3 under the V_{gs} ranging from 0V to 100V. Field-effect mobility and subthreshold slope were evaluated to be about 1.94 cm Vs^{-1} and 6.67V/decade.
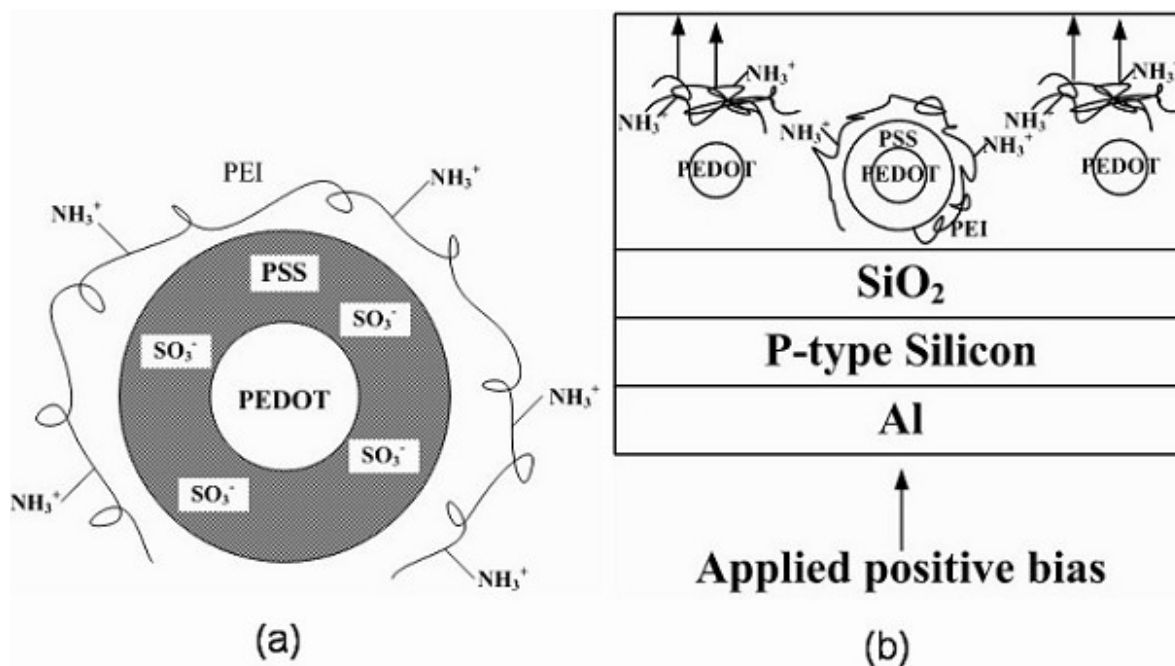

Fig 3. (a) The synthesized structure of PEDOT-PSS with PEI, (b) Operation mechanism of the depletion-mode OTFT.

In order to investigate the role of PEI, devices based on PEDOT-PSS were fabricated. Fig. 4 shows the I-V characteristics of devices without PEI. It is obvious the I-V characteristics have a resistor instead of a transistor behavior. Compared with the I-V characteristics of devices based on PEDOT-PSS with PEI, the source-drain currents of devices without PEI were larger. The low source-drain current for PEDOT-PSS-PEI based on OTFT was attributed to the $SO_3^-H^+$ groups of PSS, which were electrostatically linked with the NH_3^+ groups of PEI as the PEI was mixed with PEDOT-PSS. The charge carriers were localized in the sulfur atoms.
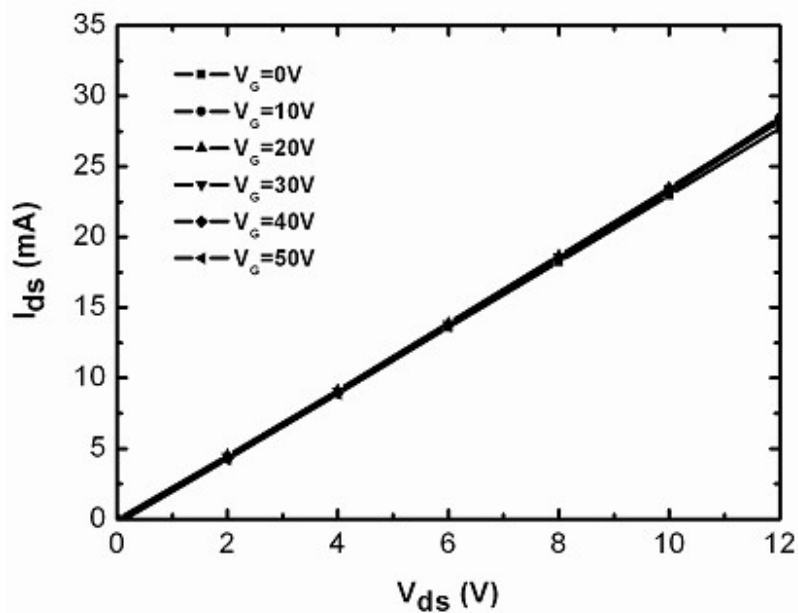
Fig 4. I-V characteristics of OTFT based on PEDOT-PSS without PEI. It only indicates the resistor.

In summary, the depletion mode of OTFTs based on PEDOT-PSS with PEI has been demonstrated. The devices with large current could be applied in electric circuits with large currents. The on/off ratio is about 10^8. Field-effect mobility and subthreshold slope were evaluated to be about 1.94 cm Vs^{-1} and 6.67V/decade. Without the incorporation of PEI in PEDOT-PSS, a very high conductivity can be observed in PEDOT-PSS which only indicates the resistor behavior. The role of the PEI in the PEDOT-PSS is found to be the key issue in modulating the layer conductivity.

Abrasion Damage of Geogrids Induced by Turbid Flow

Ching-Chuan Huang

Department of Civil Engineering, College of Engineering, National Cheng Kung University
samhcc@mail.ncku.edu.tw

ABSTRACT

A circular flow chamber is developed to study the abrasion damage of three woven geogrids. This chamber creates consistent turbid flow conditions in terms of flow velocities and particle concentrations, and is an effective tool for laboratory studies on abrasion damage of geosynthetic materials induced by turbid flows. Two types of damages on the strands of woven geogrids are identified : one is the abrasion against the surface of strands in the flow direction; the other one is the cutting of strands normal to the flow direction. The strength reductions increase with the increase of test duration, while the strength reduction rates decrease as the test duration increases. An epoxy-coated geogrid (GRID 6) appeared to have higher resistance against abrasion than a polyvinylchloride-coated geogrid (GRID 2) indicating that the use of new coating materials to increase the durability of woven geogrids in turbid flow environments is possible. This also suggests a need for establishing a standard test method to evaluate the effectiveness and robustness of coating materials.

Fig. 1 Geogrid containers used in a pilot test on seashore protection. (Huang and Liao, 2007)

BRIEF DESCRIPTION OF THE STUDY

The use of locally available construction material in infrastructure construction projects is an important part of sustainable development and environment conservation. The present study was motivated by a

damaged site in a pilot test, which uses polymeric geogrid container (as shown in Fig. 1) and gravels available on-site, as a seashore protention measure. This project presents a state-of-the-art application of polymeric materials (or geosynthetics) in a harsh environment. In this case, the geogrid is subjected to cyclic movements of gravels on the surface of geogrid container, causing abrasion damage of the geogrid, as shown in Fig. 2.
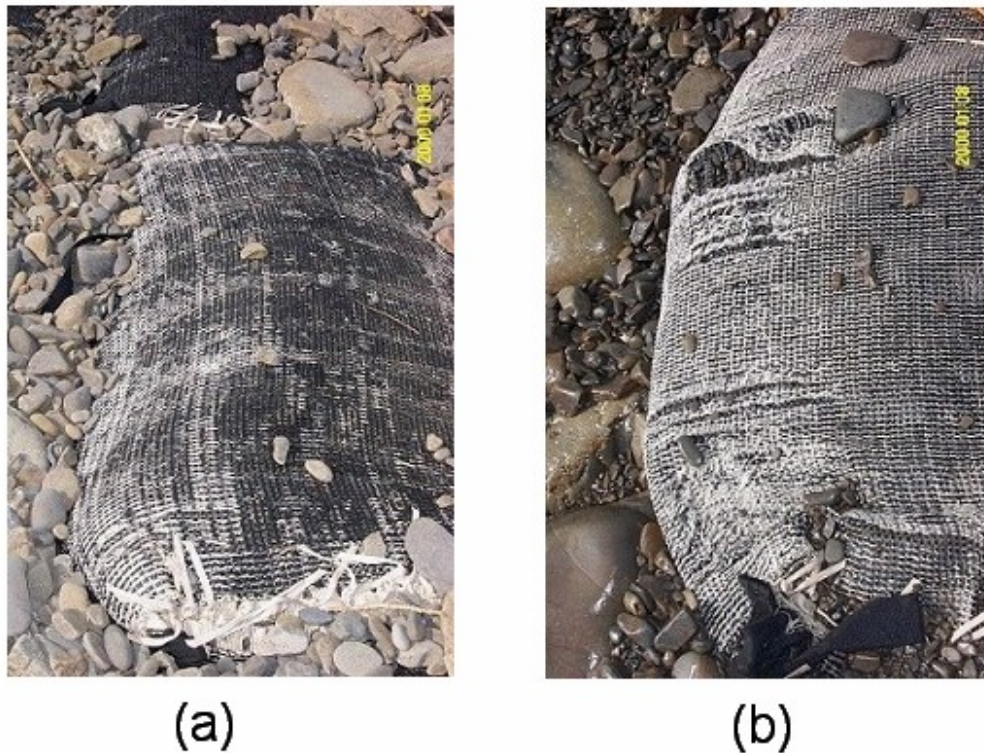

(a)　　　　　　　　　(b)

Fig. 2 Various degrees of damage on the geogrid containers observed a month after completion : (a) an example of moderate damage, (b) an example of serious damage. (Huang and Liao, 2007)

In order to simulate this type of damage in the laboratory, a circular flow chamber as shown in Fig. 3 is developed. In contrast to the conventional flume used in hydraulic engineering studies, the circular flow chamber eliminates possible problems associated with producing turbid flow condition, pumping the gravel-suspended fluid, and constructing a high-capacity water storage thank. Flow velocity measurements (Fig. 4) suggested that uniform flow velocity fields are generated along the inner surface of the chamer, as shown in Figs. 5(a) and 5(b).
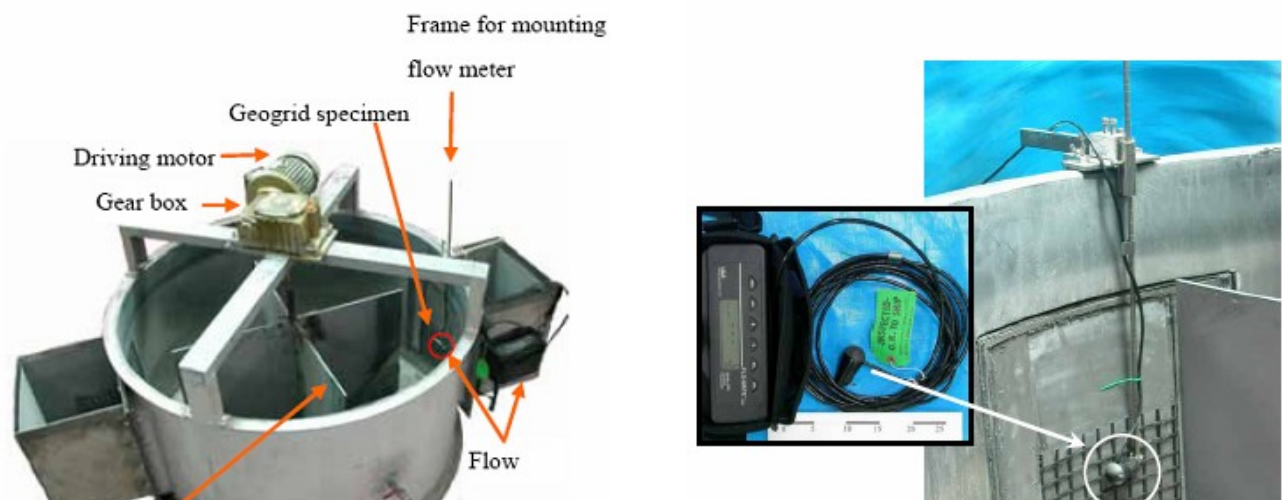
Fig. 3 1.5 m-diameter, 1.0 m-high turbid flow chamber developed in the present study. (Huang and Liao, 2007)

Fig. 4 A flow velocity measurement set-up used in the present study. (Huang and Liao, 2007)
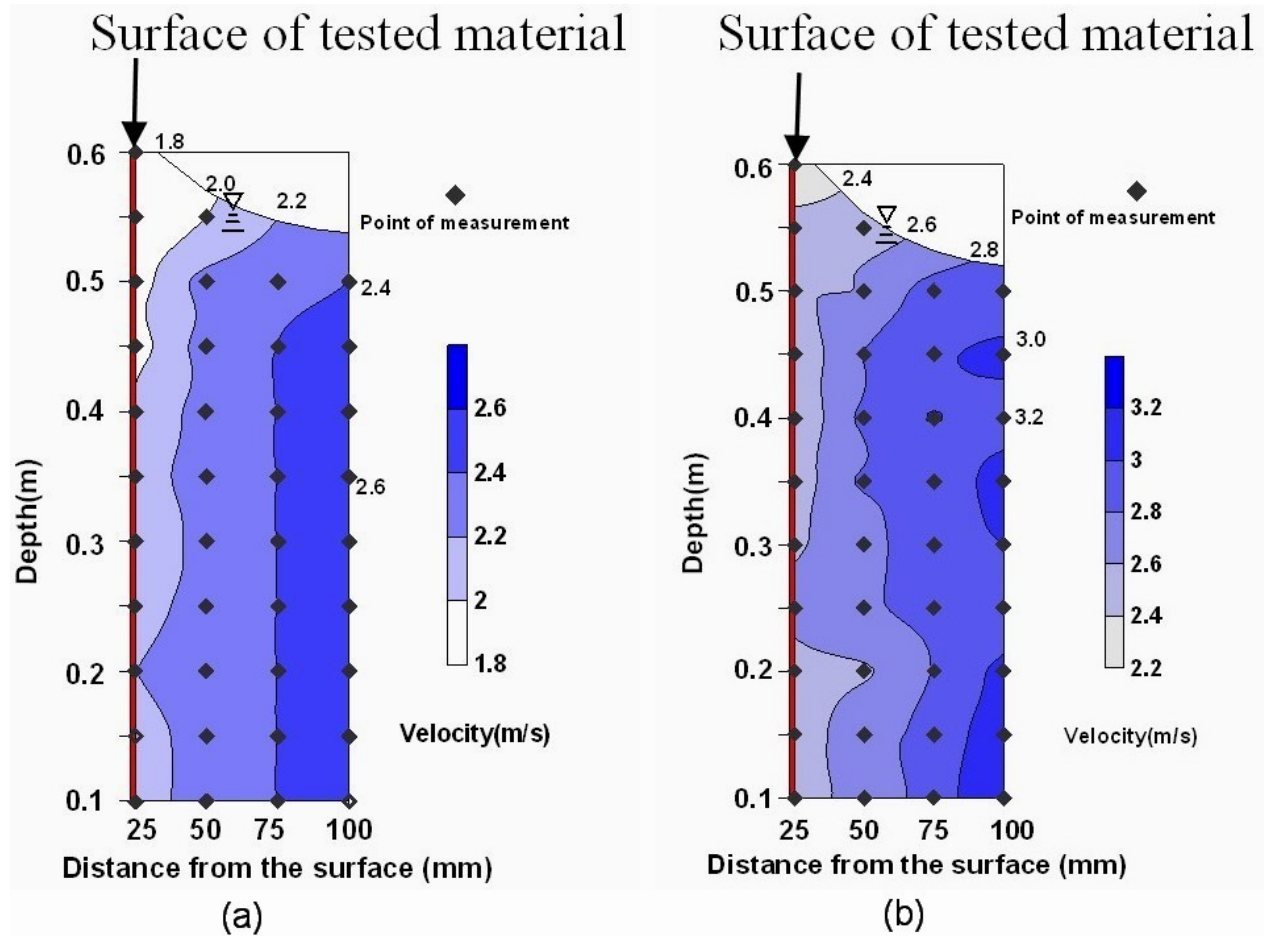

Fig. 5 (a)Measured velocity field at 40RPM (Average velocity near the surface of tested material, V_m = 2.2 m/s); (b)Measured velocity field at 50RPM (Average velocity near the surface of tested material, V_m = 2.5 m/s). (Huang and Liao, 2007)

Two types of damage were found for the geogrids tested : 1. abrasive damage of the geogrid strands in the flow direction (as shown in Fig. 6(a)), and 2. damage of the geogrid strand normal to the flow direction (as shown in Fig. 6(b)). The observed patterns of damage are in good agreement with those observed in the field, suggesting that a laboratory accelerating test is feasible in predicting geogrid damage induced by turbid flows.
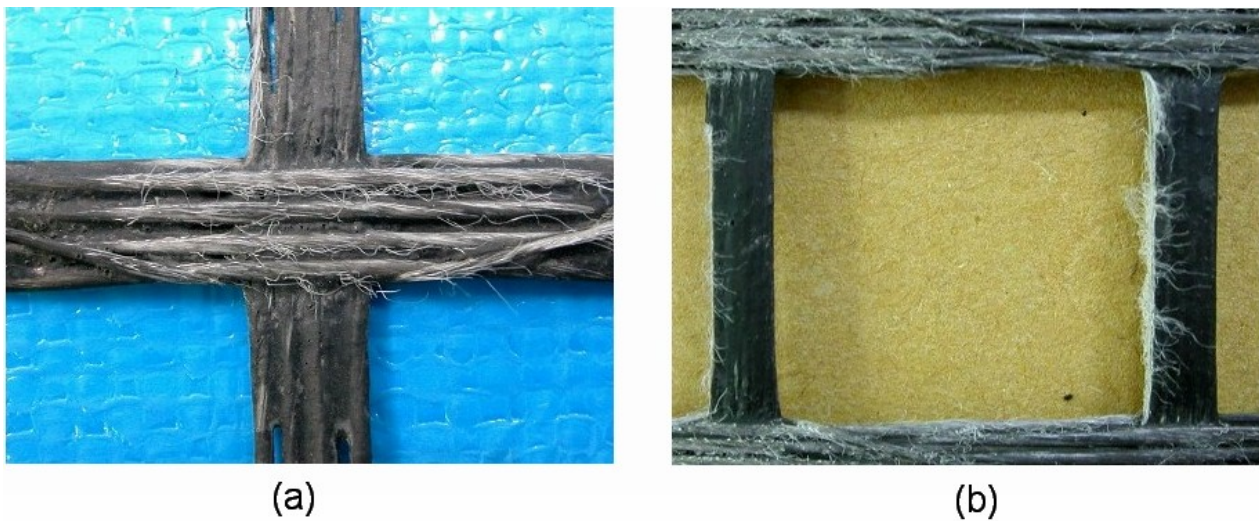
Fig. 6 Close views on the damaged geogrid (GRID2) at T = 8 hrs. : (a) a strand in machine direction, (b) strands in cross-machine direction. (Huang and Liao, 2007)

For three types of geogrids tested, extents of damage (expressed by percentage of strength loss, P.S.R.) increase linearly with the flow duration (T) for T ⬚ 24 hrs; the value of P.S.R. increase at smaller rates for T > 24 hrs., compared with those for T ⬚ 24 hrs. as shown in Fig. 7. It was also found from Fig. 7 that the geogrid coated with EPOXY (GRID 6) generally has about 20% less P.S.R. comparing with those for the geogrids coated with polyvinylchloride (PVC). This suggests that the development of abrasion-resistant material, such as the EPOXY used here, as the coating material for geogrids may play a key role in the application of polymeric geogrids in harsh environments.
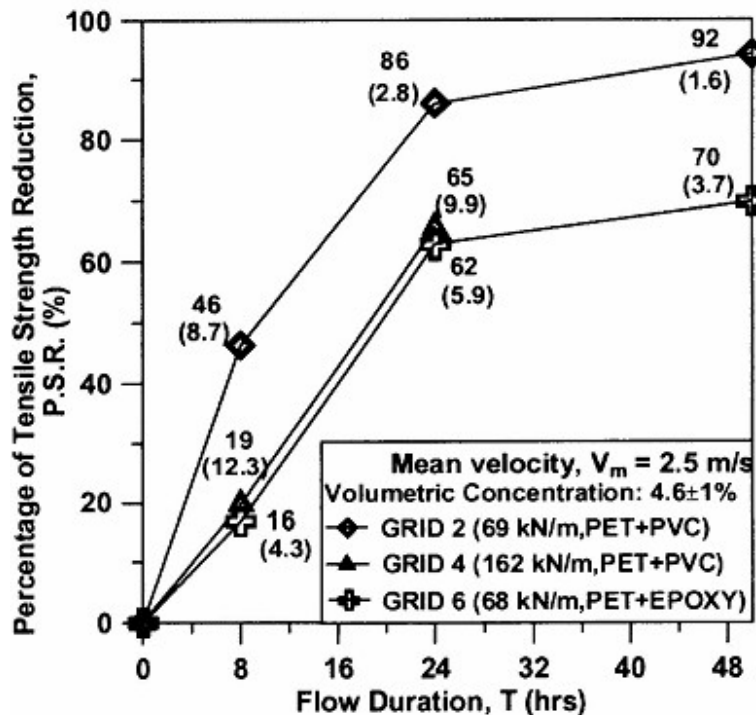

Fig. 7 P.S.R. vs. T relationships for various types of geogrids under V_m = 2.5 m/s and P_c = 4.6 ± 1 %. (Huang and Liao, 2007)

The present study investigated the effect of particle concentrations to the abrasion damage of geogrids (namely, GRID 2 and GRID 6, as shown in Figs. 8 and 9, respectively). Under typical particle

concentrations of several percents, the extent of damage can be very high within a flow duration of T = 24 hrs., again suggesting the severity of abrasion damage of geogrids in a turbid flow environment. These test results also suggested that using a higher tensile strength geogrid (with a thicker bundle of polymeric yarns) or using a high abrasion-resisting coating material, such as EPOXY, can be effective measures in reducing the extent of abrasion damage (in terms of P.S.R.) of polymeric geogrids exposed to turbid flow environments.
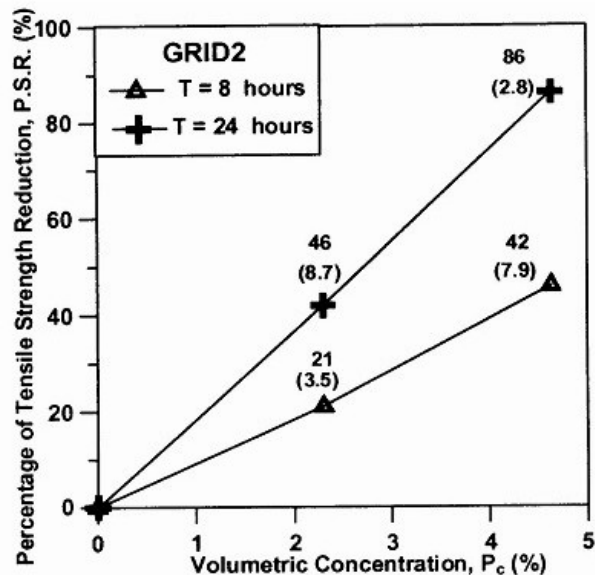
Fig. 8 Effect of particle concentrations on P.S.R. for GRID 2 under different test durations. (Huang and Liao, 2007)
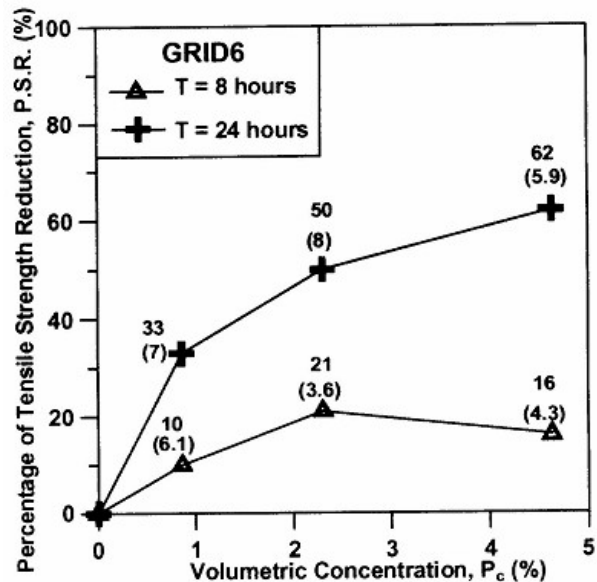

Fig. 9 Effect of particle concentrations on P.S.R. for GRID 6 under different test durations. (Huang and Liao, 2007)

The above essay is extracted from :

Huang, C.C. and Liao, C.C. (2007) "Abrasion damage of geogrids induced by turbid flow" Geotextiles and Geomembranes, Vol. 25, No. 2, pp. 128-138.

The functional insufficiency of human CD4 +CD25high T regulatory cells in allergic asthma is subjected to TNF-α modulation

Yen-Lin Lin[1,2], Chi-Chang Shieh[2,3], Jiu-Yao Wang[1,3,*]

[1]Institute of Basic Medical Sciences, College of Medicine, National Cheng Kung University, Tainan, TAIWAN
[2]Institute of Microbiology and Immunology, College of Medicine, National Cheng Kung University, Tainan, TAIWAN
[3]Department of Pediatrics, College of Medicine, National Cheng Kung University, Tainan, TAIWAN
a122@mail.ncku.edu.tw

Allergic asthma is characterized by a systemic, exacerbate Th2 cytokine immune response to environmental allergens that leads to airflow obstruction, airway hyper-responsiveness (AHR), and ongoing active airway inflammation (1). Despite recent progress in the understanding of the role of Th2 and inflammatory cytokines, such as TNF-α•(2), in the pathogenesis of the disease, the mechanism underlying the development of allergen sensitization, and more importantly, the role of the regulatory pathway in the control of allergic diseases remains unknown. Although there is extensive evidence that regulatory T cells (Treg) play a major role in controlling immune responses (3), studies exploring the role of CD4+ Treg cells in allergic diseases have primarily focused on antigen-induced IL-10 producing Treg cells (i.e. inducible Treg) (4, 5).

Thymus-derived naturally occurring regulatory T cells (nTreg) are CD4+CD25+ T cells, functionally distinguished by their capacity to limit CD4+CD25- T cell proliferation and Th1/Th2 cytokines production (6, 7). Only few studies have focused on the role of nTreg in common allergic diseases. For example, children who had outgrown their cow's milk sensitivity had significantly higher levels of CD4 +CD25+ T cells in their peripheral blood and were less responsive to stimulation with β-lactoglobulin *in vitro* than those who maintained a clinically active allergy (8). Natural Tregs have also been shown to suppress allergic responses to inhaled antigens such as grass or birch pollen (9-11). In contrast, animal studies on the role of nTregs in allergic asthma have yielded conflicting data. Although the development of AHR is unaffected by altering the number of CD4+ CD25+ Treg cells (12, 13), the development of eosinophilic airway inflammation is reported to be both increased (12), and paradoxically decreased (14), after depletion of naturally occurring CD4+ CD25+ Treg cells. This discrepancy may be due to the different genetic backgrounds of the mice studied. However, the factors that influence the functional capacity in Treg cell-mediated suppression of allergen–specific immune responses have not been delineated in allergic asthmatic patients.

Herein, we have demonstrated that the expression of Foxp3 and cell-induced suppressive activity in CD4 +CD25high regulatory T cells were significantly decreased in allergic asthmatic patients (Fig.1).
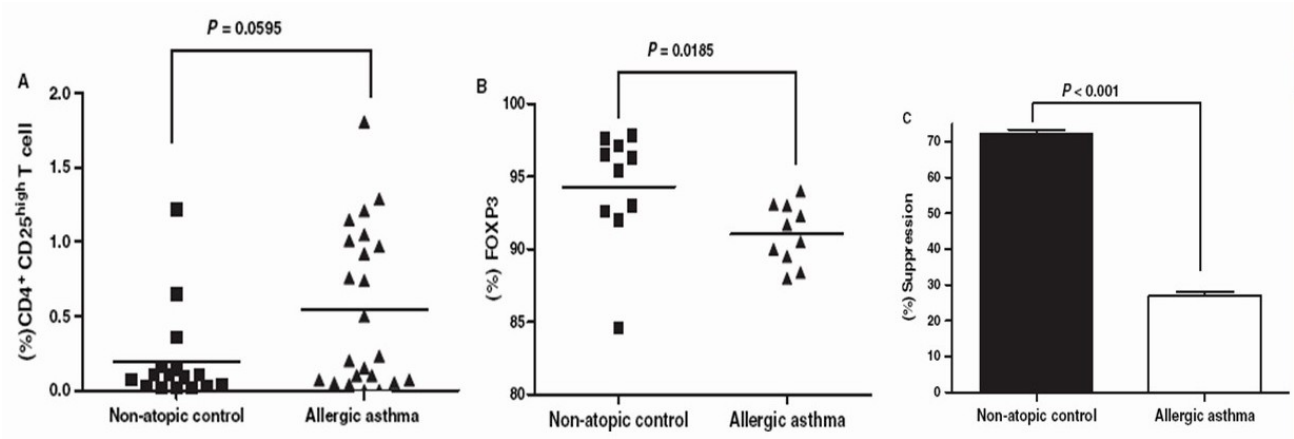
Figure 1.

We also find that TNF-α, a pleiotropic cytokine, plays a critical role in bridging innate and adaptive immunity in chronic inflammatory disease, is increased in Der p-stimulated PBMCs of allergic asthmatics, and impairs the regulatory activity of natural Treg cells via the TNF-α receptor 2 (TNFR2) signaling pathway to down-modulate Foxp3 expression (Figure 2 and 3)

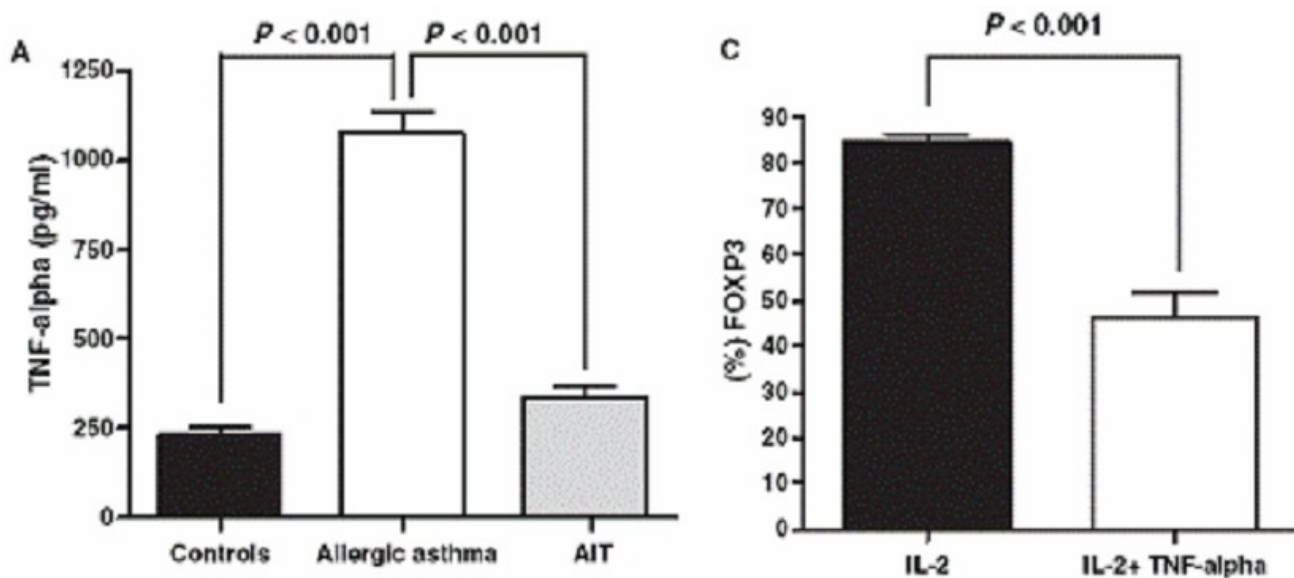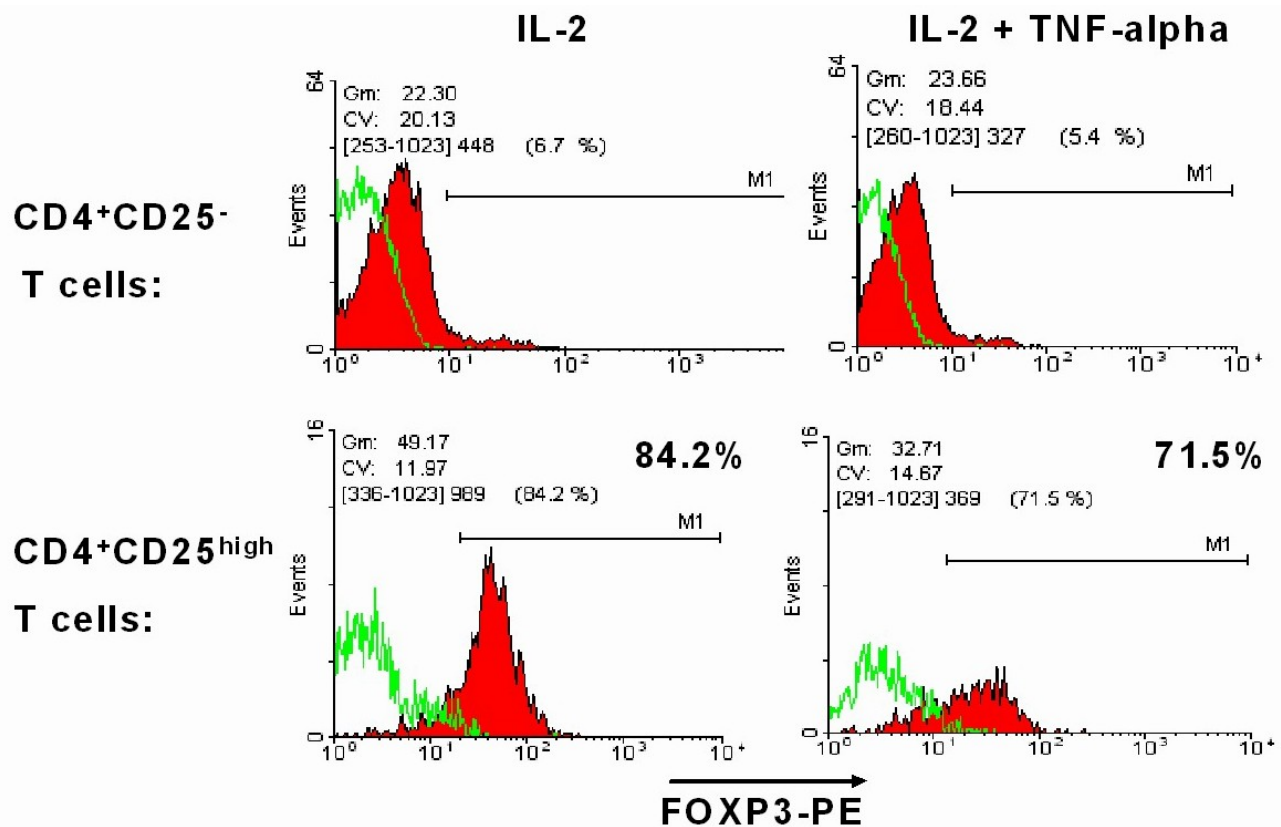
Figure 2.

Figure 3.

The addition of the soluble TNF-α receptor-IgG₁Fc fusion protein, etanercept, reversed the expression of Foxp3 and the loss of inhibitory activity of Treg cells in allergic asthmatics, which may explain, at least in part, the mechanism of functional insufficiency of natural regulatory T cells in allergic asthma (Figure 4).
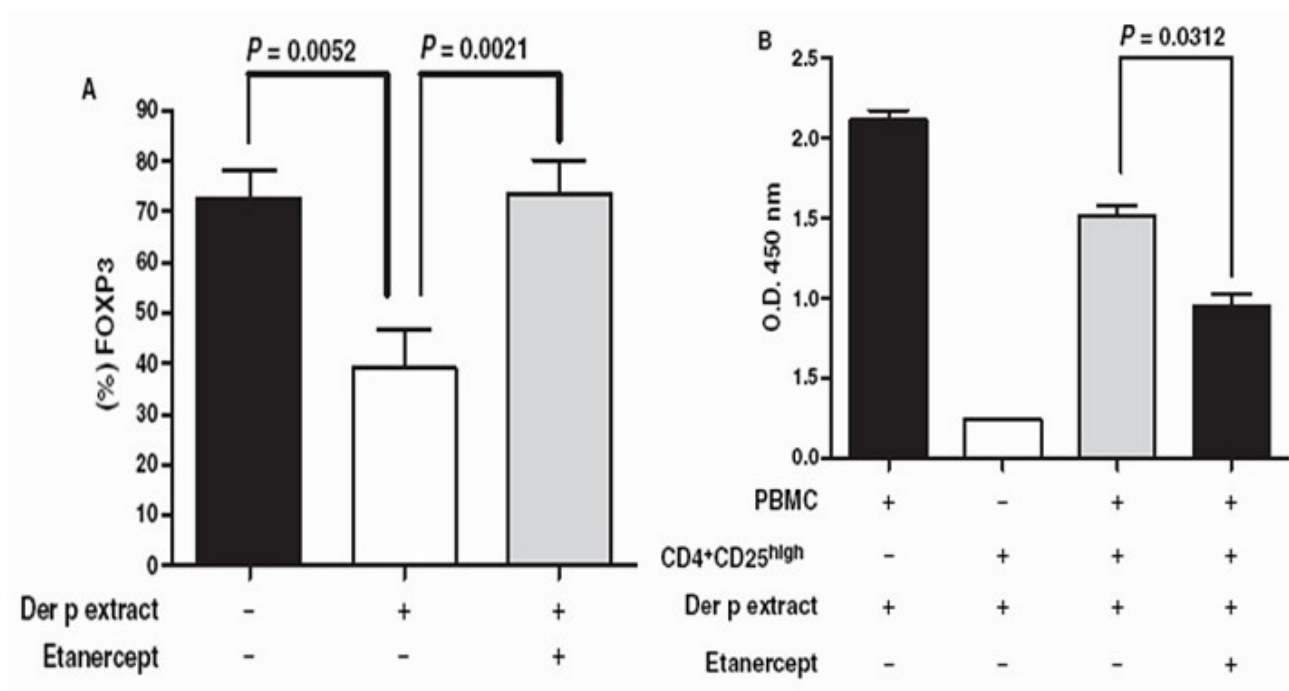

Figure 4.

In summary, we have found that functional insufficiency of natural Tregs in allergic asthma may be

related to the enhanced production of TNF-α and its effect on the Foxp3 expression in Treg cells. These results may provide a new therapeutic modality in the treatment of allergic asthma.

REFERENCES

1. Wills-Karp M. Interleukin-13 in asthma pathogenesis. Immunol Rev 2004; **202**:175–190.
2. Berry M, Brightling C, Pavord I, Wardlaw AJ. TNF-α in asthma. Curr Opin Pharmco 2007; 7:1-4.
3. Akdis M, Blaser K, Akdis CA. T regulatory cells in allergy: Novel concepts in the pathogenesis, prevention, and treatment of allergic diseases. J Allergy Clin Immunol 2005;**116**:961-8.
4. Francis JN, Till SJ, Durham SR. Induction of IL-10⁺CD4⁺CD25⁺ T cells by grass pollen immunotherapy. J Allergy Clin Immunol 2003; **111**:1255–1261.
5. Jutel M, Akdis M, Budak F, Aebischer-Casaulta C, Wrzyszcz M, Blaser K, et al. IL-10 and TGF-beta cooperate in the regulatory T cell response to mucosal allergens in normal immunity and specific immunotherapy. Eur J Immunol 2003; **33**:1205–1214.
6. Sakaguchi S. Naturally arising Foxp3-expressing CD25⁺CD4⁺ regulatory T cells in immunological tolerance to self and non-self. Nat Immunol 2005; **6**:345–352.
7. Coombes JL, Robinson NJ, Maloy KJ, Uhlig HH, Powrie F. Regulatory T cells and intestinal homeostasis. Immunol Rev 2005; **204**:184–194.
8. Karlsson MR, Rugtveit J, Brandtzaeg P. Allergen-responsive CD4⁺CD25⁺ regulatory T cells in children who have outgrown cow's milk allergy. J Exp Med 2004; **199**:1679–1688.
9. Ling EM, Smith T, Nguyen XD, Pridgeon C, Dallman M, Arbery J, Carr VA, et al. Relation of CD4⁺CD25⁺ regulatory T-cell suppression of allergen-driven T-cell activation to atopic status and expression of allergic disease. Lancet 2004; **363**:608–615.
10. Grindebacke H, Wing K, Andersson AC, Suri-Payer E, Rak S, Rudin A. Defective suppression of Th2 cytokines by CD4⁺CD25⁺ regulatory T cells in birch allergics during birch pollen season. Clin Exp Allergy 2004; **34**:1364–72.

English

Interactions between Poly(*N*-vinylformamide) and Sodium Dodecyl Sulfate As Studied by Fluorescence and Two-Dimensional NOE NMR Spectroscopy

Jung-Kai Tzeng, Sheng-Shu Hou*

Department of Chemical Engineering, National Cheng Kung University
sshou@mail.ncku.edu.tw

The interactions between water-soluble polymers and surfactants have been extensively studied for more than four decades. The mixed polymer/surfactant systems are of interest not only because of many prevalent and hopeful applications such as pharmaceutical formulation, food products, detergency, paints and inks, improved oil recovery, etc., but also because of the nature of interaction between the polymer and surfactant, especially the issue concerned about the concentration far below the regular critical micelle concentration (cmc) of surfactant.

N-vinylformamide (NVF) has been able to commercially produced lately. The NVF-based polymers have been considered as possible substitutes for the polymers, which are made from the acrylamide (AA) that is now widely known as a possible carcinogen. Besides, NVF is easily polymerizable and copolymerizable with other acrylic monomers by means of conventional free radical polymerization. Additionally, poly(vinylamine) can be simply prepared through acidic or basic hydrolysis of PNVF. NVF-based materials have been proved applicable for some industrial fields to be taken in many applications, such as inorganic oxide hybrid materials, papermaking, coating slips, petroleum recovery, hair care, and the drag reducing polymers. Moreover, fundamental researches about NVF are of interest recently. However, no study about the interactions between PNVF and anionic surfactant SDS has been reported.

In the present study, we investigate the interaction between water-soluble and uncharged PNVF and the anionic surfactant SDS in terms of pyrene fluorescence and the 2D NOESY experiments. In addition, the correlation between the bulk solution properties obtained from pyrene fluorescence and the cooperative association behavior of surfactant to the polymer chain, which could be obtained using the 2D NOESY, is the main purpose of this study. As seen in figure 1, the cmc of SDS is about 8 mM in the absence of PNVF. Above the cmc of SDS, the I_1/I_3 values are between 1.1 and 1.2 which are consistent with the reported literature. The location and distribution of pyrene molecules in the solution can be obtained from the I_E/I_M ratios. For the pure SDS solution in figure 1b, as [SDS] are lower than the cmc of SDS, the I_E/I_M ratios maintain a value (≈ 0.011) and do not change with [SDS]. As the [SDS] just higher than the

cmc of SDS, pyrene molecules are solubilized into the SDS micelles. At the same concentrations, the I_E/I_M ratio reaches the peak value as observed (≈ 0.025). After that, the number of SDS micelles drastically increases as SDS is continuously added into solution, but the total pyrene concentration in the solution remains the same ([pyrene] $\approx 1.0 \times 10^{-6}$ M). Therefore, the pyrene molecules are averagely dispersed in a large number of micelles, leading to that the I_E/I_M ratios drop to the low values again.
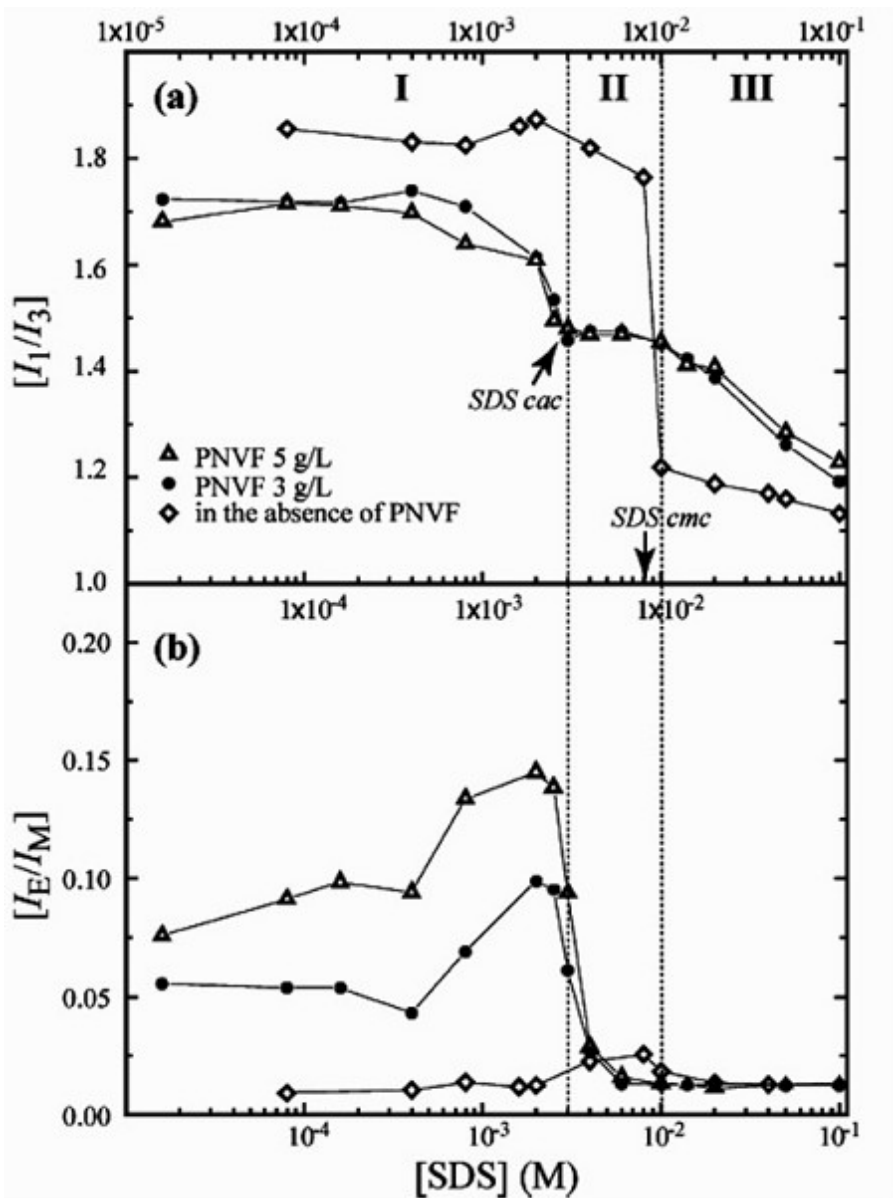

Fig 1. Correlation pictures between (a) I_1/I_3 and (b) I_E/I_M of pyrene solubilized in water ( ), 3 g/L PNVF ( ), and 5 g/L PNVF (●) aqueous solutions and concentration of SDS. The cac of SDS (ca. 3 mM) in the presence of PNVF is taken as the onset of the plateau in region II.

The correlation plots between the I_1/I_3 ratios of PNVF/SDS and [SDS] could be divided into three regions. In region 1, the I_1/I_3 ratios are independent of [SDS] and maintain a low value about 1.7. As [SDS] higher than 0.4 mM, I_1/I_3 ratios begin decreasing slowly. Obviously, the I_1/I_3 ratios of 5 g/L PNVF solution which are between 0.075 and 0.095 are larger than the ones of 3 g/L PNVF solution(≈ 0.050). Besides, the PNVF/SDS solutions have higher I_E/I_M ratios but lower I_1/I_3 ratios than the pure SDS

solution. It indicates that dissolved PNVF chains form the microdomains which are less polar than the bulk water phase. Further, the I_E/I_M ratios of the PNVF/SDS solutions are larger than the ones for pure SDS solution at the cmc of SDS. It indicates that more pyrene molecules can be solubilized into the polymer coils than into the polymer-free SDS micelles.
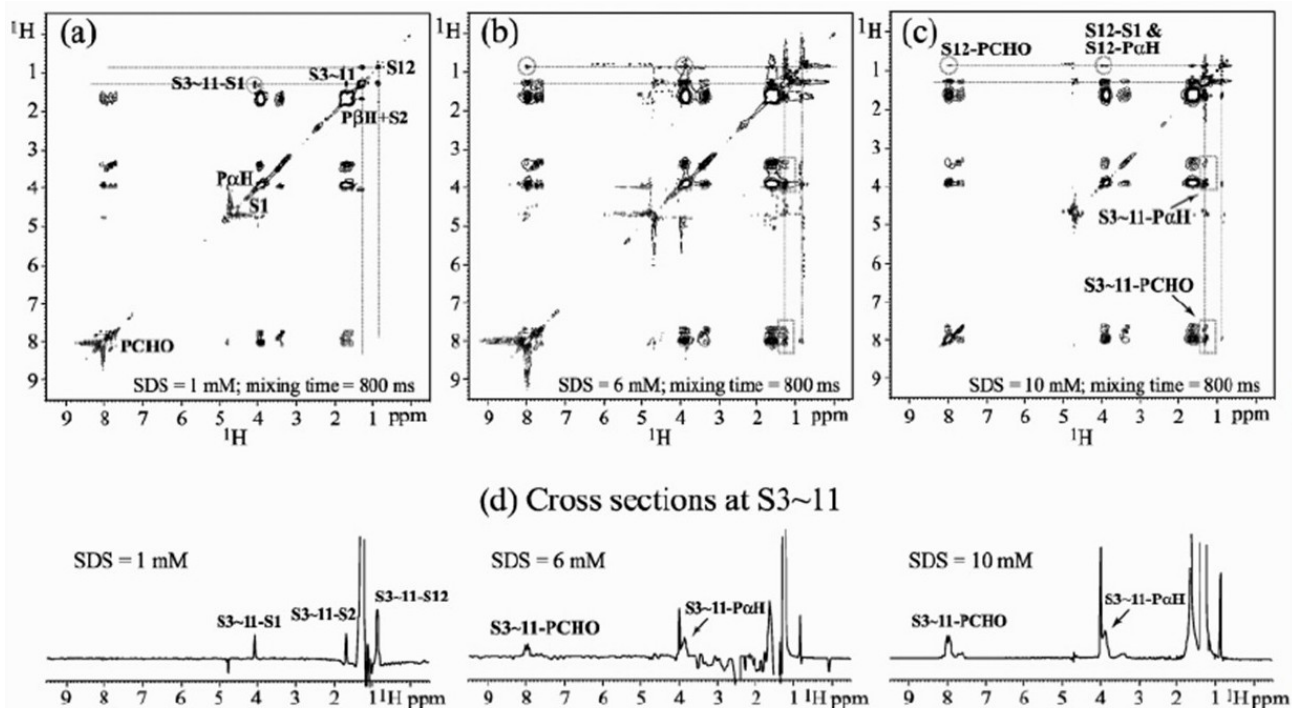

Figure 2. ^{1}H-^{1}H 2D NOESY spectra for the PNVF/SDS/D$_2$O solutions at 1 mM (a), 6 mM (b), and 10 mM (c) of SDS. The mixing time is 800 ms, and the contour levels in the spectra are linearly spaced. The cross-peaks are in phase with the diagonal peaks. (d) The cross section taken at S3~11 along the ω_2 from each 2D spectrum. The cross-peaks shown in the 2D spectra and 1D cross sections clearly indicate that alkyl protons of SDS are in close contact (<0.5 nm) with polymer chains.

According to the figure 2a, there is no cross-peak between PNVF and SDS, showing that at [SDS] = 1 mM which is the midpoint of the first I_1/I_3 reduction in region I, the SDS molecules don't approach (within 0.5 nm) the polymer chains closely. At the same time, SDS molecules probably start to form aggregates, but it is not necessarily that PNVF-SDS aggregates form at the low [SDS]. The results are similar to the PVP/SDS system, in which the reduction of the I_1/I_3 ratio starta at [SDS] below the accepted cac. Up to now, there is no proper explanation.
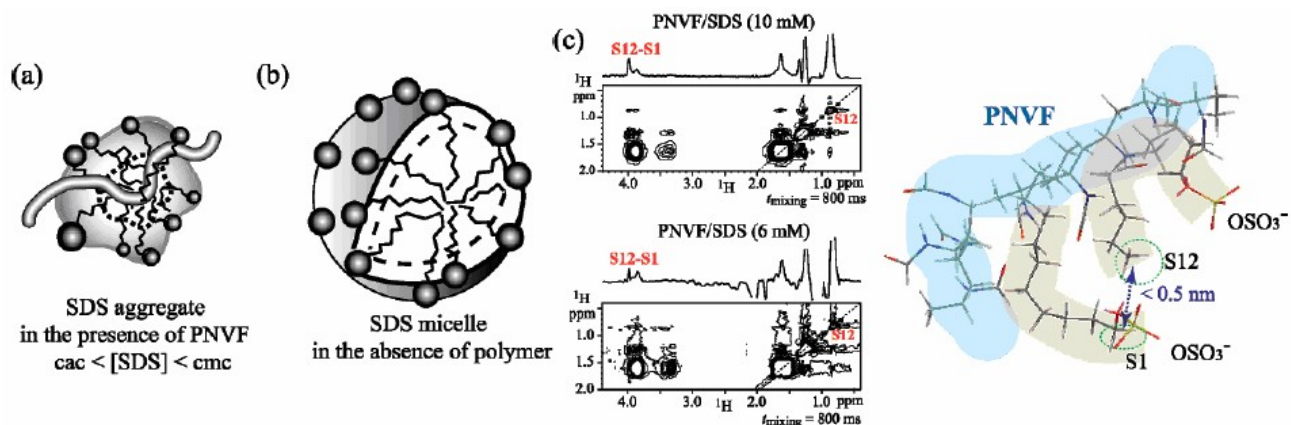
Figure 3. (a) An illustration of the complex structure of PNVF-induced SDS aggregate. (b) An illustration of the structure of a spherical SDS micelle. (c) Visualization of the possible structure (right) of surfactant molecules in the vicinity of the PNVF as deduced from the cross-relaxation effects in the 2D NOESY spectra (left). The 1D spectrum above the 2D spectrum is the cross section at S12 in the ö2 dimension. The cross-peak between S12 and S1 is due to the intermolecular interaction of the SDS molecules.

In figure 3a, we propose the structure of SDS aggregates bound on the PNVF chains as a result of the cross-relaxation obtained by the 2D NOESY experiments. First, the SDS alkyl chain in the PNVF-SDS aggregates is more curly than in the pure SDS micelle in figure 3b. The sulfate group is away from the polymer chain because no correlation between S1 and polymer protons is seen in the 2D NOESY spectra. Because of the curled alkyl chain of SDS and perturbational polymer chain, the curled alkyl chain of SDS is partially associated with polymer chain. We except the sulfate head groups are not closely packed and not forming a spherical surface, which is like that of the pure SDS micelle. The PNVF-induced SDS aggregate has a ragged surface with water. In other words, some SDS molecules protrude into the bulk water phase and some with curly alkyl chains are closer to the polymer chain. As showed in figure 3c, the supramolecular structure of PNVF-SDS complex, the folded conformation of SDS leads to the intermolecular cross relaxation between S12 and S1, which is observed in the 2D NOESY spectra ([SDS]) 6 and 10 mM).